JOURNAL OF GEOPHYSICAL RESEARCH, VOL. 86, NO. C5, PAGES 4089–4102, MAY 20, 1981

HF Radar Measurements of Long Ocean Waves

B. J. LIPA,[1] D. E. BARRICK,[2] J. W. MARESCA, JR.[1]

Sea-echo data from three separate narrow-beam HF radar experiments on the Pacific Ocean are analyzed here by techniques presented in Lipa and Barrick (1980). Only those wave spectral components whose periods exceeded 10 s were included. Close agreement of radar-deduced wave field parameters with surface observations confirms the validity of the second-order theoretical solution for the echo Doppler spectrum, upon which this analysis is based. Depending on the particular experiment, a variety of wave parameters are extracted, including rms wave height, mean wave direction, dominant period, angular spread of the wave field, the nondirectional wave height spectrum, and higher Fourier angular coefficients versus wave frequency. The radar-deduced wave parameters fall within the combined error bounds estimated for the radar and buoy wave observations; consequently, we contend that the primary source of error for radar data is finite sample size. Typical accuracies for specific parameters resulting from observations averaged over a 2-hour period are ±5% for wave height, ±0.5 s for wave period, and ±7° for wave direction. Hence the utility of HF radars for long-wave measurements has been validated.

1. INTRODUCTION

Ever since theoretical derivations related the ocean wave height directional spectrum to the second-order sea-echo HF (high-frequency) Doppler spectrum [*Barrick*, 1971, 1972; *Hasselmann*, 1971], the prospect of measuring important sea-state parameters at a single radar operating frequency has enticed radio oceanographers. However, the nonlinear nature of the integral equation containing the wave height directional spectrum appeared sufficiently formidable that no immediate solutions were demonstrated. *Barrick and Lipa* [1979*a*] and *Lipa and Barrick* [1980] trace the evolution of approximations and techniques that permit extraction of sea-state parameters from second-order echo; in this paper, we restrict our attention to demonstration of inversion techniques via three separate experiments yielding long-wave directional parameters, and we compare all results with alternate sea-surface wave observations.

First-order sea echo originates from those components of the ocean-wave spectrum of length equal to half the radar wavelength. This echo appears in the received Doppler spectrum as distinct narrow peaks whose symmetrical shifts from the radar frequency are related to the phase velocity of these short waves (at 25 MHz—a typical HF frequency—the first-order Bragg echo originates from 6-m long ocean waves whose phase velocity is 3.06 m/s and temporal period is ~2 s); these echoes are referred to as the first-order 'Bragg' peaks or lines. Surrounding these Bragg peaks in Doppler space is a continuum. This continuum is the second-order sea echo that we employ here to extract long-wave directional parameters. The agreement of these experimental data with alternate observations, shown subsequently, demonstrates that the second-order theoretical solution correctly describes this portion of the echo.

The second-order solution is obtained by using boundary perturbation techniques on the Navier-Stokes hydrodynamic equations and Maxwell's electromagnetic equations at the free-water surface. Interpretation of the solution shows that a double Bragg interaction produces this portion of the echo, as indicated by the appearance of the wave height spectrum twice in the integrand of the solution. It should be stressed that these equations for the second-order echo contain neither arbitrary parameters nor mathematical models that must be determined by fits to measured data. Hence these expressions are unique solutions for second-order scatter and are employed with no modifications or adjustments to force agreement with data.

Thus far, only three groups have actually analyzed the second-order portion of experimental HF data. *Barrick* [1977] and *Maresca and Georges* [1980] developed and demonstrated approximations that permit extractions of significant wave height and its nondirectional spectrum. *Lipa* [1978] was the first to attempt an inversion of the integral equation to obtain directional information about the wave field. All of those works produced results that agreed favorably with alternate sea-surface measurements. However, those works have been based on approximations and/or models for the wave field that limit their utility for most commonly encountered situations. This paper employs none of these restrictions and hence demonstrates the general feasibility of second-order extraction/inversion. The data analyzed herein have the following general properties: (1) They originate from experiments where narrow antenna beams were employed (i.e., <25°), and (2) we restrict our attention to the 'long-wave' region of the ocean spectrum, which we define here to be those wave components whose periods exceed 10 s.

All of the techniques used in this paper for extracting long-wave information from second-order Doppler echo were derived, analyzed, and presented in *Lipa and Barrick* [1980], hereinafter cited as L-B. We draw on these expressions below, with a minimum of mathematical detail; the reader is referred to L-B for greater derivation and explanation. In brief, the Doppler spectrum is analyzed as follows: If sharp spikes occur in the higher-order structure adjacent to the first-order lines, one is justified in testing the hypothesis of an ocean spectral model with a single dominant wavelength. Analysis begins with the assumption that this model is unidirectional; if statistical tests show that such a model does not adequately fit the data, parameters of a more general cardioid model are derived. When the higher-order structure is continuous in nature, even the cardioid model will fail the maximum-likelihood test of its applicability; then a general inversion procedure is employed to give Fourier coefficients of the ocean wave spectrum as a function of ocean wave frequency.

[1] Remote Measurements Laboratory, SRI International, Menlo Park, California 94025.
[2] Wave Propagation Laboratory/ERL, National Oceanic and Atmospheric Administration, Boulder, Colorado 80303.

Paper number 80C1337.
0148-0227/80/080C-1337$01.00

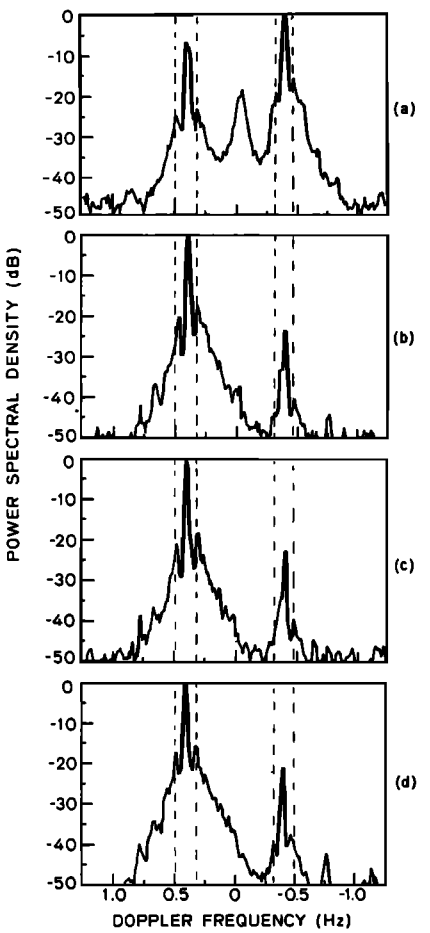

Fig. 1. Examples of 84-sample power spectra recorded at Warf May 17, 1978: (*a*) 1628 UT, (*b*) 1703 UT, (*c*) 1724 UT, (*d*) 1822 UT. The dashed lines indicate the frequencies of the swell peaks. Note that these are obscured at the two intermediate times.

Thus, choice of the final analysis method is dictated by an objective consideration of the radar data and its statistics.

Data from three experiments are analyzed. Two originated from 'ground-wave' radars (i.e., where the signal propagates along the sea to the scattering patch and back). The third experiment involved a 'skywave' radar, in which the signals propagated via ionospheric paths, to arrive at the scattering area over 1500 km away. The nature of the ocean waves producing the second-order echo analyzed subsequently varied considerably among the three experiments. At one extreme the echo was produced by a narrow band of waves in frequency called 'swell.' At the other extreme the ocean spectrum was quite spread in frequency so that a simple swell model would not explain the echo; in this case, full integral inversion was employed.

We have compared the radar results with all available surface observations and have included estimates of the uncertainty in every result so that meaningful comparisons can be made. The most stringent test is the comparison between radar and buoy measurements, since the uncertainties are low. We also include wave hindcasts, although these are less useful for purposes of quantitative comparisons because of large uncertainties.

2. SRI Skywave Experiment

On May 17, 1978, skywave radar observations were made of the North Pacific, near the location of the NOAA data buoy at 41°N, 138°W by using the SRI Wide Aperture Research Facility located in central California. The radar receiving antenna is 2.5 km in length and operates between 6 and 30 MHz, forming multiple beams of width 0.5° at 15 MHz. The radar can be electronically steered with azimuth increments of 0.25° to a limit of ±32° from an east-west boresight. In this experiment, transmission occurred at a frequency of approximately 15 MHz via a single reflection from the ionosphere during stable sporadic-E conditions.

Radar Spectra

High quality backscatter was observed from three locations near the buoy and at four time periods between 1600 and 1800 UT. Spectral broadening of the skywave radar echoes caused by multipath and by smearing were minimal in this data set because of the extremely stable ionosphere. At each location, data was taken from 21 contiguous range cells of width 3 km and from 4 adjacent azimuths spaced by 0.25°. These spectra were incoherently averaged without normalization to give 14 84-sample averages covering 102.4 s in time from an area about 60 km × 63 km. Figure 1 gives examples of echo Doppler spectra measured in each time period. According to the theory of L-B, narrow-band ocean swell produces four sharp spikes in the second-order spectrum that are approximately symmetrically displaced from the first-order lines. All four spikes appear in spectra measured around 1628 and 1822 UT, but at the intermediate times (around 1703 and 1724 UT), the structure of the swell peak on the inner side of the weaker first-order line is concealed by another echo of greater magnitude. This spurious echo lies too close to the Bragg line to be due to second-order scatter from ocean waves and is believed to be due to splitting of the first-order line by ionospheric multipath, a problem in skywave ocean observations [*Maresca and Georges,* 1980]. This belief is supported by the reduction of the remaining first-order energy relative to the other swell peak. In many cases, a distinct peak cannot be resolved (see Figure 1). When this problem occurs, we have not used this spectral region in the analysis.

Data Analysis and Results

L-B describe several techniques of increasing complexity that may be applied to the peaks of the second-order spectrum to yield estimates of parameters describing the swell. For this experiment the simplest technique provided a good fit to the data; the swell is modeled as having a single wave number and direction with a contribution to the directional ocean-wave spectrum at wave number k and direction θ given by

$$S(k, \theta) = H_s^2 k^{-1} \delta(k - k_s) \delta(\theta - \theta_s) \quad (1)$$

where H_s, θ_s, k_s are the rms wave height, direction and wave number of the swell, respectively. This model was applicable because the observed swell had a narrow distribution in both angle and wave number; in addition, the radar beamwidth was small.

L-B show that the four swell peaks occur at angular frequencies given by

$$\omega_{m,m'} = m\omega_s + m'[\omega_B^4 + 2m\omega_s^2\omega_B^2 \cos \theta_s + \omega_s^4]^{1/4} \quad (2)$$

In this expression the indices m and m' define the swell peaks: m' is 1 or −1 for positive or negative Doppler frequency, m is 1 or −1 for the outer or inner side of the Bragg line, and ω_s and ω_B are the swell and first-order Bragg frequencies defined by

$$\omega_s = \sqrt{gk_s} \qquad \omega_B = \sqrt{2gk_0} \quad (3)$$

TABLE 1. Analysis of Skywave Radar Data (May 17, 1978)

Time	Period From (5), s	Radar/Swell Angle, deg			rms Wave Height From (9), cm			
		From (6)	From (8)	From (8)	$m = m' = +1$	$m = m' = -1$	$m = 1, m' = -1$	$m = -1, m' = 1$
1628	11.9	133	130	54	59	52	56	55
1630	12.6	136	140	68	52	44	46	48
1703	11.8	75				44		46
1705	11.9	128				47		50
1707	12.3	103				37		43
1708	12.2	149				34		41
1710	12.6	101				33		40
1712	12.8	180				37		49
1713	13.1	156				38		43
1725	11.9	180				33		35
1726	11.8	156				35		45
1728	11.4	180				40		44
1730	11.6	141				34		37
1823	12.8	113	150	46	47	46	46	46

where k_0 is the radar wave number and g is the gravitational acceleration. Estimates of swell wave number, period, and direction follow from the relations

$$k_s = (\Delta\omega^+ + \Delta\omega^-)^2/16g \tag{4}$$

$$T_s = 2\pi/\sqrt{gk_s} \tag{5}$$

$$\theta_s = \cos^{-1}\left[\frac{8\omega_B(\Delta\omega^+ - \Delta\omega^-)}{(\Delta\omega^+ + \Delta\omega^-)^2}\right] \tag{6}$$

where $\Delta\omega^+$ and $\Delta\omega^-$ are the radian frequency displacements between the swell peaks surrounding the approaching and receding Bragg lines.

The ratio $R_{m,m'}$ of the energy in a swell peak to that in the neighboring first-order line is given by

$$R_{m,m'} = 2H_s^2|\Gamma_{m,m'}(k_s, \theta_s)|^2 \tag{7}$$

where $\Gamma_{m,m'}$ is the coupling coefficient defined in L-B. The rms wave height and the angle θ_s follow from a maximum-likelihood analysis in which the following expression is minimized:

$$\sum_{m,m'=\pm 1} \frac{(R_{mm'} - 2H_s^2|\Gamma_{mm'}|^2)^2}{\text{Variance}\,(R_{m,m'})} \tag{8}$$

The peak energy was calculated by integrating the spectrum between the half-power points; the frequency was taken as the centroid of the spectrum in this frequency range. Thus we minimized the sum of weighted squared deviations of the experimental values of $R_{m,m'}$ from the ideal functional form to give optimum values of $\hat{\theta}_s$ and $\hat{H}_s$. The residual $I(\hat{\Theta}_s, \hat{H}_s)$ obeys an approximate χ^2 distribution, and a χ^2 test demonstrated the validity of the ocean-wave spectral model (1).

When four uncontaminated swell peaks were available in the radar spectrum, the peak frequencies were analyzed to give swell direction and wave number. This wave number was then used in an analysis of peak amplitudes to give wave height and an independent estimate of direction. As a consistency check we also computed the rms waveheight from each swell peak by using the formula

$$H_s = \left(\frac{R_{m,m'}}{2\,|\Gamma_{m,m'}|^2}\right)^{1/2} \tag{9}$$

substituting the calculated direction and wave number. If the model for the directional ocean wave spectrum given by (1) provides a good fit to the data, the four values of wave height given by (9) should be consistent.

When one swell peak was contaminated, (4), (5), and (6) were applied with $\Delta\omega^+$ replaced by $2\Delta\omega$, where $\Delta\omega$ is the frequency displacement of the uncontaminated peak from the first-order line. Because the weaker first-order line is split, neither of the ratios $R_{m,1}$ is known with certainty, and there is insufficient information in the remaining two ratios to determine both wave height and angle with adequate accuracy. Instead, we used the direction determined from the uncontaminated spectra and obtained two estimates of wave height by applying (9) to the peaks surrounding the stronger uncontaminated Bragg peak.

Results of the analysis are shown in Table 1. The major source of uncertainty is the unknown ionospheric perturbations. The accuracy of the derived results was estimated from the consistency between independent estimates.

Comparison with Surface Data

The nature and extent of the weather systems affecting the measurement area are shown on the surface charts given in Figure 2. The radar measurements were made in the center of

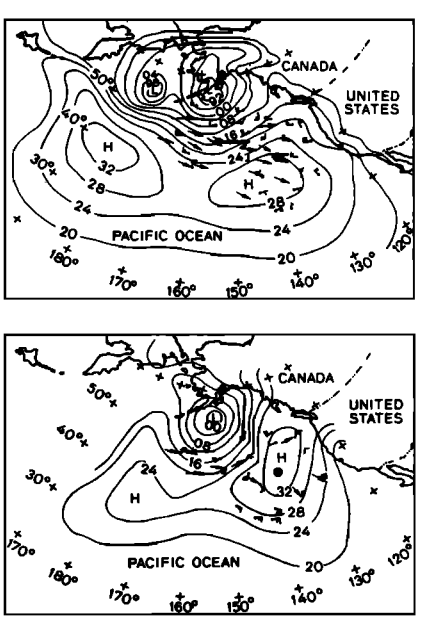

Fig. 2. National Weather Service surface charts compiled for May 17, 1978 (top) 0000 UT, (bottom) 1800 UT. The location of the NOAA Data Buoy 46006 is indicated by the solid circle.

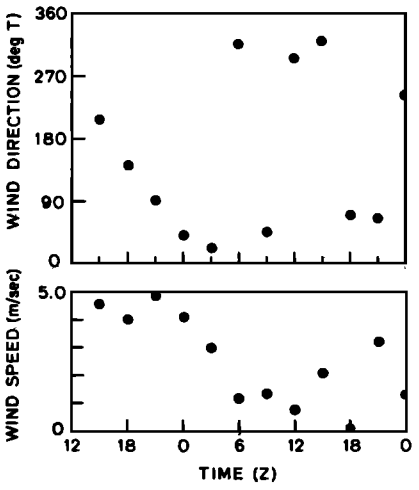

Fig. 3. Wind speed and direction measurements made at the data buoy between 1200 UT, May 16 and 0000 UT May 18, 1978.

a large high-pressure system, with ocean waves in the vicinity consisting primarily of swell generated by distant low-pressure centers to the north and west, with minimal wind waves.

To verify the radar results, we used the 3-hourly measurements of winds and nondirectional spectra made by the NOAA data buoy, the ship reports of swell direction provided by the National Weather Service, and the hindcast tables prepared by OSI, Inc. Figure 3 gives a time history of local wind velocity at the buoy over the 24 hours preceding the experiment. Winds were extremely light and reversed direction during the experimental period. This is indicated in the radar spectra by a reversal in the relative magnitude of the approaching and receding Bragg lines between 1628 and 1703 UT (see Figure 1). Ocean wave spectra recorded by the buoy are shown in Figure 4. These spectra contain low-frequency peaks characteristic of ocean swell. To obtain wave height estimates for comparison with the radar results, the spectra were integrated over the same frequency band used to compute peak energies in the radar spectra, which in this case includes essentially all the energy in the ocean-wave spectrum. The swell period was taken to be the centroid frequency of the spectrum in this band.

Estimates of swell direction were obtained from ship observations made between 1800 UT, May 16, and 1800 UT, May 17, provided in surface charts. Unfortunately, there were no observations made near the site of the radar measurements. Therefore, a hindcast was made of the direction of swell passing within 4° of latitude at the buoy longitude. We assumed that the swell propagated along a great circle path at its group velocity, which was calculated from the period measured by the buoy. The original ship reports are given in Table 2 with the calculated swell direction, latitude, and time of arrival. We also compared our results with a hindcast made by OSI, Inc., based on the methods of *Pierson et al.* [1953]. The estimated swell directions obtained independently from the two hindcasts are entirely consistent.

The comparison between the surface data and swell parameters derived from the radar data is shown in Table 3. The initial entries are the averaged radar results for each time period selected in the following manner: at 1628 and 1822 UT we used the estimates of wave height and direction derived from the maximum likelihood analysis, as they were the most stable to measurement uncertainty. At 1703 and 1724 UT we used the direction derived from the frequency estimates and the averaged estimate of wave height from the two uncontaminated swell peaks. The next entry in Table 3 gives the means and rms deviations for the four time periods and finally we give the in situ observations, which were essentially constant over the experimental period. The radar and in-situ observations agree to within 1 cm in rms wave height, 3° in direction, and 1 s in period. The uncertainties in buoy estimates given in Table 3 follow from specifications given by *Withee and Blasingame* [1976], and uncertainties in hindcast values were made by using methods described in Appendix A. These uncertainties are sufficient to explain the small discrepancies between radar and surface observations.

3. San Clemente Island Experiment

In this NOAA/NRL/ITS experiment, surface-wave measurements of sea echo were made from San Clemente Island off the coast of California on December 4, 1972 [*Barrick et al.*, 1974]. The radar was located on the northwest side of the island and looked westward into the Pacific, transmitting simultaneously on 10 frequencies from 2.41 to 24.1 MHz. The receiving antenna was a broadside array 260 m in length with a one-way beamwidth ranging from 15° at 3 MHz to 7° at 24 MHz. The receiving antenna formed two simultaneous beams pointed along the directions 240°T and 270°T; the system recorded data simultaneously from three range cells centered 22.5, 30, and 37.5 km from the receiver.

Radar Spectra

Data were processed and were recorded digitally as 204.8-s coherent spectra; nine consecutive spectra were summed to cover a period of approximately 30 m at the start times 1014, 1114, 1525, and 1608 PST. To combine data from different range cells, account must be taken of the fact that data signals from the greater ranges are weaker because the path loss is greater. We used a logarithmic normalization scheme developed by *Barrick* [1980] to average data multiplied by an unknown factor, such as path loss; this technique is described briefly in Appendix B. In applying this method to the experimental data, an estimate of the additive noise power level was made by averaging spectral values at large Doppler shifts, where the sea-echo signal is negligible. We then determined the frequency bounds (ω_1 and ω_2) of the useful part of the echo spectrum, which was defined as having a signal/noise ratio that exceeds 10. The Doppler spectrum $\sigma(\omega)$ from each range cell was normalized by the factor

$$\exp\left\{\left[\int_{\omega_1}^{\omega_2} \ln \sigma(\omega)\, d\omega\right] \Big/ (\omega_2 - \omega_1)\right\} \qquad (10)$$

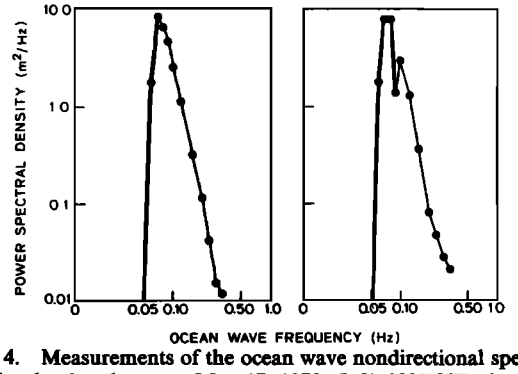

Fig. 4. Measurements of the ocean wave nondirectional spectrum made by the data buoy on May 17, 1978, (left) 1800 UT, significant wave height 2.17 m, (right) 1500 UT, 2.13 m.

TABLE 2. Hindcast of Swell Direction at Longitude 138°W From Individual Ship Reports

Ship Reports of Swell Direction					Hindcast of Swell Direction at 138°W		
Latitude, °N	Longitude, °W	Date, May 1978	Time, UT	Swell Direction, deg T	Latitude, °N	Time, UT	Swell Direction, deg T
42	148.5	16	1800	300	36.9	2000	307
48.5	154	16	0000	300	39.6	1600	311
46	147	16	1800	300	41.7	1600	307
46	145	17	0000	300	42.8	1700	305

and the normalized spectra summed to give a composite spectrum consisting of approximately 27 independent sample averages (nine from time averaging, three from range averaging).

We analyzed data for radar transmitter frequencies between 5 and 15 MHz, because in this frequency range the radar signal/noise ratio is large and there is pronounced second-order structure owing to swell and wind waves. This includes the following frequencies: 6.9, 9.4, 13.40, 13.41, and 13.43 MHz. Spectra at the latter three closely spaced frequencies were averaged to increase the effective number of degrees of freedom by another factor of 3. An example of a measured power spectrum is given in Figure 5, showing small peaks owing to ocean swell between the first-order lines and the wind-wave peaks. It is evident from this spectrum that the wind-wave peaks are dominant in the second-order spectrum; a better idea of the relative magnitude of swell versus wind-wave peaks follows from Figure 6 which shows the spectra from different range cells drawn on a linear scale.

Methods and Results

The calculation of the frequencies and amplitudes of the swell spectral peaks was more complicated than for the previous experiment because the wind-wave echoes were predominant in the second-order spectrum. However, the swell region was normally well separated from the rest of the spectrum (as seen in Figure 6) and we reduced the small contribution to the swell energy from the first-order and wind-wave peaks by subtracting parabolae fitted to the neighboring 'walls.' The energy and centroid frequency were then calculated between the half-power points as before.

In the late afternoon at the higher radar frequencies, the swell and wind-wave peaks merged together because the wind wave height increased from 1.5 to 2.5 m under the influence of a 16-m/s wind onset; for this reason we did not use the 13.4 MHz data for the last period of the afternoon (better resolution and signal-to-noise ratio inherent in more modern HF radar systems—exemplified in the other two recent experiments—would have permitted discrimination of the two peaks even for the afternoon period).

The second-order spectrum at negative Doppler frequencies is almost always below the additive noise which was determined from the data as was described previously. We therefore modified the methods of L-B to apply to the data measured only at positive Doppler frequencies for the two beam positions. In the following discussion, we term the beams from 270°T and 240° as the 'right' and 'left' beams, respectively; parameters associated with the beams are identified by superscripts R and L.

We began, as for the previous experiment, assuming ocean swell with a directional ocean-wave spectrum modeled as an impulse function in direction and wave number (as in (1)). In place of (2) for the peak frequencies we have

$$\omega_{m,1}{}^{R} = m\omega_s + (\omega_B{}^4 + 2m\omega_s{}^2\omega_B{}^2 \cos\theta_s + \omega_s{}^4)^{1/4} \quad (11)$$

$$\omega_{m,1}{}^{L} = m\omega_s + \left(\omega_B{}^4 + 2m\omega_s{}^2\omega_B{}^2 \cos\left(\theta_s + \frac{\pi}{6}\right) + \omega_s{}^4\right)^{1/4} \quad (12)$$

and in place of (7)

$$R_{m,1}{}^{R} = 2H_s{}^2\,|\Gamma_{m,1}(k_s, \theta_s)|^2 \quad (13)$$

$$R_{m,1}{}^{L} = 2H_s{}^2\left|\Gamma_{m,1}\left(k_s, \theta_s + \frac{\pi}{6}\right)\right|^2 \quad (14)$$

We obtained maximum-likelihood estimates of period and direction from (11) and (12) and of wave height and direction from (13) and (14). Statistical uncertainties in these parameters were obtained from the random surface-height statistics, using the theory of linear error propagation, applied by L-B, section 3, to a similar problem. Results of this analysis are shown in Table 4: There is a consistent discrepancy between the swell direction derived from (11) and (12) and from that derived from (13) and (14), which exceeds the statistical standard deviation by about a factor of 10. It, therefore, follows

TABLE 3. Comparison of Warf Radar-Swell Parameters with Surface Data

Source	Location (°N, °W)	Time, UT	H_s, cm	θ_s, deg T	T_s, s
Radar	(40,137)	1628	51	325	12.3
	(38,137)	1703	42	322	12.4
	(38,139)	1724	38	286	11.7
	(38,137)	1822	46	300	12.8
Mean Values					
Radar	(38,137)	1719	44 ± 3	308 ± 8	12.3 ± 0.2
Buoy	(41,138)	1650	45 ± 20		13.3 ± 1.5
Ship report	(40,138)	1725		305	
Hindcast	(41,138)	1800	30 ± 20	305 ± 8	11 ± 1.1

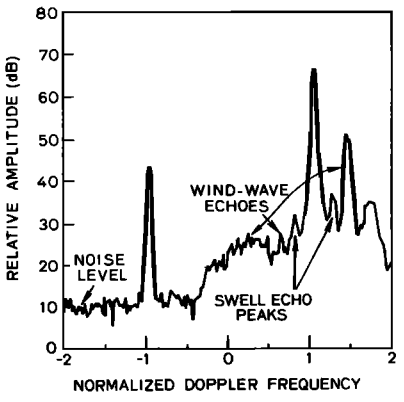

Fig. 5. An example of a 9-sample average power spectrum measured at San Clemente Island, December 4, 1972, 1114–1156 PST, radar frequency 9.4 MHz, frequency resolution 0.005 Hz.

that the impulse-function model for a single swell component does not provide a good fit to the data.

As was described by L-B, if the swell peaks are discrete, but a unidirectional model does not fit the data, we assume a model with a single swell wavelength but with a finite spread in angle having a cardioid distribution; this model for the directional ocean-wave spectrum is given by

$$S(k, \theta) = H_s^2 k^{-1} \delta(k - k_s) \cos^s\left(\frac{\theta - \theta_s}{2}\right) \Big/ A(s) \qquad (15)$$

where

$$A(s) = \int_{-\pi}^{\pi} \cos^s(\theta/2)\, d\theta = 2\sqrt{\pi}\, \Gamma\left(\frac{s}{2} + \frac{1}{2}\right) \Big/ \Gamma(s/2 + 1) \qquad (16)$$

The corresponding peak frequencies are the same as those for the previous model given in (11) and (12), but expressions for the energy ratios $R_{m,m'}$ have the modified form

$$R_{m,1}{}^R = \frac{2H_s^2}{A(s)} \int_{-\pi}^{\pi} |\Gamma_{m,1}(\theta)|^2 \cos^s\left(\frac{\theta - \theta_s}{2}\right) d\theta$$

$$R_{m,1}{}^L = \frac{2H_s^2}{A(s)} \int_{-\pi}^{\pi} \left|\Gamma_{m,1}\left(\theta + \frac{\pi}{6}\right)\right|^2 \cos^s\left(\frac{\theta + \frac{\pi}{6} - \theta_s}{2}\right) d\theta \qquad (17)$$

Maximum-likelihood estimates of wave height, direction, and the spreading parameter s were obtained by least squares fitting (17) to the data. These values are shown in Table 4; the swell direction derived from maximum likelihood is also inconsistent with results obtained by using the peak frequencies, and it therefore appears that a model of the ocean surface containing a single swell component is unable to provide an adequate description of the data.

We therefore assumed a model spectrum consisting of the sum of two impulse functions representing swell arriving from two directions, θ_1 and θ_2:

$$S(k, \theta) = H_1^2 k^{-1} \delta(k - k_1)\delta(\theta - \theta_1) + H_2^2 k^{-1} \delta(k - k_1)\delta(\theta - \theta_2) \qquad (18)$$

Theoretically, this ocean-wave spectrum produces eight spikes in the radar spectrum; however, for the San Clemente experiment only four can be resolved because of finite swell bandwidths and beamwidths. The corresponding centroid frequency for the right beam representing the combination of the two swell peaks that cannot be individually resolved is

$$\omega_{m,1}{}^R = \frac{H_1^2 |\Gamma(\theta_1, k_1)|^2 \eta_1 + H_2^2 |\Gamma(\theta_2, k_2)|^2 \eta_2}{H_1^2 |\Gamma(\theta_1, k_1)|^2 + H_2^2 |\Gamma(\theta_2, k_2)|^2} \qquad (19)$$

where η_1 is the peak frequency corresponding to the first swell component given by $m\omega_1 + (\omega_B^4 + 2m\omega_1^2\omega_B^2 \cos\theta_1 + \omega_1^4)^{1/4}$ with $\omega_1 = \sqrt{gk_1}$ and similarly for η_2. The total energy ratio is given by

$$R_{m,1}{}^R = 2H_1^2 |\Gamma(\theta_1, k_1)|^2 + 2H_2^2 |\Gamma(\theta_2, k_2)|^2 \qquad (20)$$

Similar formulae apply to the left beam with the angles θ_1, θ_2 replaced by

$$\theta_1 + \frac{\pi}{6} \qquad \theta_2 + \frac{\pi}{6}$$

We attempted to use (19) and (20) together with the corresponding equations for the left beam to determine the parameters describing the two swell components. However, there was insufficient information in the data to allow so many parameters to be resolved with adequate accuracy. We, therefore, compared results from a single composite swell analysis with surface data. Later we describe results of a consistency check which shows that two swell components with the hindcast properties would produce a radar spectrum that is reasonably consistent with the measured data.

Comparison with Surface Data

A Waverider buoy moored in the scattering area provided the nondirectional ocean-wave spectrum for the periods 1015–1210 PST and 1569–1734 PST. These spectra, shown in Figure 7, contain broad swell peaks separated in frequency from a saturated wind-wave spectrum.

Because the buoy output provided no directional information, it was supplemented by wave hindcast tables prepared by OSI, Inc., available for 1000 and 1600 PST. The hindcast of swell properties given in Table 5 indicates the presence of two swell components with a total rms wave height increasing by 50% from morning to afternoon. This is in contrast with the buoy measurement of the same quantity which is almost constant throughout the day. For comparison, a composite hindcast wave height was determined as the sum of squares of the individual wave heights. The other composite values were obtained by weighting the individual components with the

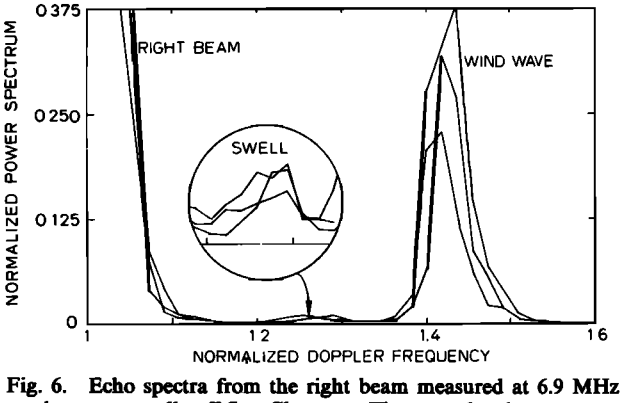

Fig. 6. Echo spectra from the right beam measured at 6.9 MHz from three range cells off San Clemente. The second-order spectrum is normalized by the first-order energy. This figure demonstrates the relative magnitude of the swell and wind-wave peaks.

TABLE 4. San Clemente Island Swell Parameters Assuming a Single Swell Component

Time, PST	Radar, Frequency, MHz	Frequency Analysis		Amplitude Analysis				
				Impulse Function Model		Finite Angle Model		
		Period, s	Angle, deg T	Angle, deg T	rms Wave Height, cm	Angle, deg T	rms Wave Height, cm	Spreading Factor, s
1014–1042	6.9	13.7 ± 0.05	230 ± 3	270 ± 4	17.9 ± 1.0	280	20.7	18
	9.4	13.2 ± 0.03	245 ± 2	275 ± 4	16.8 ± 0.8	290	20.5	14
	13.4	13.2 ± 0.05	215 ± 2	265 ± 2	14.7 ± 0.3	270	16.5	18
1114–1156	6.9	13.1 ± 0.03	240 ± 2	270 ± 4	15.6 ± 0.7	280	17.8	14
	9.4	12.6 ± 0.02	250 ± 2	260 ± 5	16.1 ± 0.6	260	18.5	10
	13.4	12.8 ± 0.01	245 ± 2	265 ± 2	16.7 ± 0.3	260	19.1	14
1525–1556	6.9	12.5 ± 0.04	235 ± 2	260 ± 5	17.1 ± 0.8	270	21.2	8
	9.4	12.2 ± 0.02	260 ± 2	270 ± 4	18.1 ± 0.8	290	23.3	8
	13.4	12.6 ± 0.02	240 ± 2	270 ± 2	18.1 ± 1.0	290	23.0	10
1608–1639	6.9	13.0 ± 0.04	235 ± 2	265 ± 5	18.4 ± 1.0	280	23.2	8
	9.4	12.9 ± 0.08	215 ± 3	170 ± 4	17.1 ± 0.7	290	22.0	8

mean-square wave height; thus the composite direction follows from the formula:

$$\theta = \frac{H_1^2\theta_1 + H_2^2\theta_2}{H_1^2 + H_2^2} \tag{21}$$

with a similar formula for ocean-wave frequency.

Table 6 gives the comparison between surface data and the radar results for this 'composite' swell analysis; radar data have been averaged over transmitter frequency and time. Estimates of period from the different sources agree to within 1 s. The most reliable radar estimates of wave height and direction follow from the use of the cardioid directional model which makes allowance for angular spread: These directions agree with the surface data to within 20°; estimates of wave height agree to within 10%, except the hindcast value in the afternoon which is about 30% greater than both buoy and radar values.

Consistency Check for Two Swell Components

In this test we substituted hindcast periods and angles for the two swells into (19) and (20) for the centroid frequency and amplitude of the smeared peak in the radar spectrum. We then derived least squares estimates of the radar-deduced wave heights H_1 and H_2; these are given in Table 7. The values derived independently from different sets of radar data are quite consistent; these were averaged for comparison with hindcast values and are shown in Table 8. The agreement is fair considering the uncertainties in hindcast values in the afternoon, when the hindcast growth in wave height of the first swell component is observed neither by the radar nor by the buoy.

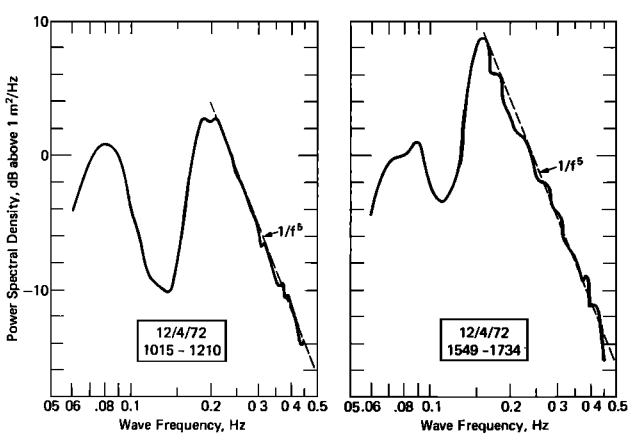

Fig. 7. Wave height nondirectional spectrum for seas west of San Clemente Island during different stages of development by 13.4 m/s westerly winds. The saturation constant for both is $\alpha = 0.011 \pm 0.0014$. Spectra have resolution of 0.01 Hz with 128 degrees of freedom.

4. PESCADERO EXPERIMENT

In this experiment, surface-wave measurements were made by Stanford University on January 19, 1978, from Pescadero on the California coast. The coherent pulse-Doppler radar operated simultaneously on four frequencies (6.8, 13.4, 21.8, and 29.8 MHz) and recorded data from four range cells 7.5 km wide, ranging from 6 to 31.5 km from the receiver. The water depth over the radar scattering region was approximately constant at 65 m. The transmitting antenna was a vertical half-rhombic approximately 250 m long and 45 m high at the apex, supported by a helium-filled balloon; the receiving antenna was a wideband loop. The beam pointed northwest into the Pacific with a half-power beamwidth of 25° at 13 MHz. A pitch-and-roll buoy operated by R. Stewart of Scripps was moored in the scattering region to provide direct surface observations to compare with the radar observations, which were also compared with visual observations and a hindcast of wave and swell conditions.

Radar Spectra

Data were processed and recorded digitally to produce 2048-s coherent spectra. Adjacent time series were overlapped by 50%, giving 23.5% correlation between sequential frequency spectra. Figure 8 shows examples of echo spectra from different range cells. The spectra taken at 6.9 MHz were often contaminated by interference from a neighboring commercial band and were excluded from the analysis. Owing to propagation loss—which increases with the radar frequency—the signal/noise ratio of the echo from the furthest range cells was

TABLE 5. Hindcast of Swell Conditions (San Clemente Island December 4, 1972)

	Swell 1		Swell 2	
Time, PST	1000	1600	1000	1600
rms wave height, cm	17	26	11	11
Period, s	15	14	12	12
Direction, deg T	255	255	303	303

TABLE 6. Comparison with Surface Data Assuming One Swell Component (San Clemente Island)

Source	rms Wave Height, cm		Direction, deg T		Period, s	
	Morning	Afternoon	Morning	Afternoon	Morning	Afternoon
Radar frequency			238	237	13.1 ± 0.01	12.6 ± 0.02
Radar amplitude (impulse function model)	16.3 ± 0.6	17.8 ± 0.7	268 ± 2	267 ± 2		
Radar amplitude (finite angle model)	18.9	22.5	273	284		
Hindcast	20.2 ± 2.5	28.2 ± 2.5	270 ± 12	263 ± 12	13.6 ± 1.2	13.5 ± 1.3
Buoy	21 ± 0.7	21.4 ± 1.5			12.5 ± 1.5	11.8 ± 1.5

sometimes inadequate; the remaining spectra were normalized logarithmically (Appendix B) and were summed; spectra measured over a period of 1 hour were incoherently averaged, and finally the frequency resolution was reduced by a factor of 5 by averaging five adjacent spectral points. The number of independent samples in the resulting spectra ranged from 50 at 29.8 MHz to 150 at 13.4 MHz. As the radar operating frequency increased, the spectra became increasingly smeared owing to sensitivity to smaller-scale current turbulence, nonlinear wave-wave interactions, and systems effects. For this reason, we did not analyze the spectral amplitudes measured at 29.8 MHz, although we did use the peak frequencies which are less sensitive to smearing.

The region close to the carrier frequency contains spurious signals (see Figure 8) that may be the result of antenna motion modulating the direct signal arising from feedback and land reflection. These signals do not, however, affect the spectrum in the region of the swell peaks.

Analysis and Results

Large-amplitude, long-period waves resulted in strong higher-order structure close to the first-order lines. The analysis of this data set was more complicated than the two considered previously for two reasons: (1) The dominant ocean waves were effectively in shallow water at 65 m depth, and (2) the ocean waves were generated too close to the radar site to be considered true swell. There is no clear separation in the measured data between a swell region and the rest of the spectrum, as with the San Clemente Island data analyzed above; for this reason, simple swell models were inapplicable, and the data were analyzed by complete integral inversion. The half-power width of the first-order peak defines the intrinsic frequency resolution, since the first-order spectrum is ideally an impulse function but in practice is smeared over a finite-frequency band by current turbulence and system effects. Before analysis we smeared the second-order spectrum over this frequency band and normalized by the first-order energy, forming the spectrum

$$R_{m,m'}(\omega_c) = \frac{\int_{\omega-\delta/2}^{\omega+\delta/2} \sigma^{(2)}(\eta)\, d\eta}{\int_{m\omega_B-\delta/2}^{m\omega_B+\delta/2} \sigma^{(1)}(\eta)\, d\eta} \tag{22}$$

where δ is the half-power width of the first-order line and ω_c is the centroid frequency of the spectrum in the frequency range $\omega - \delta/2$ to $\omega + \delta/2$.

Frequency analysis. Use of the simplest impulse-function model for swell discussed in L-B requires the assumption that all the radar spectral peaks are produced by the same ocean-wave component. In shallow water of depth d, (4) and (6) become

$$k_s \tanh (k_s d) = (\Delta\omega^+ + \Delta\omega^-)^2/16g \tag{23}$$

$$\theta_s = \cos^{-1}\left[\frac{8\omega_B(\Delta\omega^+ - \Delta\omega^-)}{(\Delta\omega^+ + \Delta\omega^-)^2} \tanh (k_s d)\right] \tag{24}$$

Table 9 gives the period and direction for the different times and radar frequencies, with standard deviations computed by using (17) and (18) of L-B.

Integral inversion. The second-order echo structure has the form of a continuum indicating a broad distribution in wave number. L-B describe a method to interpret such spectra; the ocean wave spectrum is expanded as a Fourier series in angle with coefficients that are functions of wave number.

$$S(k, \theta) = [c_0(k) + c_1(k) \cos\theta + c_2(k) \cos 2\theta + \cdots + c_{-1}(k) \sin\theta + c_{-2}(k) \sin 2\theta + \cdots]/2\pi \tag{25}$$

The first three even Fourier coefficients are then obtained by integral inversion of the second-order spectrum. Figure 9

TABLE 7. Wave Height of Two Swell Components (San Clemente Island)

Time, PST	Radar Frequency, MHz	H_1, cm		H_2, cm	
		From (19)	From (20)	From (19)	From (20)
1014–1042	6.9	14.1	14.8	15.6	15.3
	9.4	12.1	12.4	14.2	11.9
	13.4	12.7	13.2	10.6	11.1
1114–1156	6.9	12.2	12.6	13.9	14.5
	9.4	14.7	9.9	15.2	10.5
	13.4	12.0	12.5	12.7	13.2
1525–1556	6.9	15.7	16.6	10.6	11.0
	9.4	15.0	16.1	13.9	13.3
	13.4	14.0	16.7	15.9	16.0
1608–1639	6.9	15.9	16.5	13.7	13.8
	9.4	14.1	14.5	13.3	14.0

TABLE 8. Two Swell Components: Consistency Check with Hindcasts (San Clemente Island)

Source	rms Wave Height, cm			
	Swell 1		Swell 2	
	Morning	Afternoon	Morning	Afternoon
Radar frequencies	13	16	15	12
Radar amplitudes	14	17	15	12
Hindcast	17	26	11	11

shows the Fourier coefficients derived from the 13.4-MHz data plotted against ocean-wave frequency. The zero-order coefficient c_0 is identically the spatial nondirectional spectrum, but the higher-order coefficients must be interpreted further to give ocean-wave parameters that can be physically understood. *Barrick and Lipa* [1979*b*] show how the normalized directional coefficients c_1/c_0 and c_2/c_0 may be interpreted in terms of a cardioid model for the angular distribution $[\cos^s(\theta - \theta_0/2)]$ to give the mean wave direction θ_0 and the spreading factor s. The half-power beamwidth is then given by

$$\Delta\theta = 4\cos^{-1}[(\tfrac{1}{2})^{1/s}] \tag{26}$$

and is shown with the mean-wave direction in Figure 9.

Temporal spectra shown in Figure 10 were derived from the nondirectional coefficient, using the formula

$$F(f) = \sqrt{g}\left[\frac{4\pi k^{3/2} c_0(k)}{\sqrt{\tanh(kd)} + kd\,\mathrm{sech}^2(kd)/\sqrt{\tanh(kd)}}\right] \tag{27}$$

where f is the ocean-wave frequency. L-B describe how standard deviations in the derived ocean parameters are obtainable from the known sea-surface height statistics; we show examples of these uncertainties in Figure 11.

For values of k/k_0 less than 0.04, the inversion method becomes unstable with large uncertainties in c_0 and c_2. This problem occurs because the constant Doppler frequency contours are almost circles in (k, θ) space and the coupling coefficient is approximately proportional to $\cos^2\theta$; the second-order radar cross section therefore depends on c_0 and c_2 only through the combination $c_0 + (c_2/2)$. For the 20-MHz data in the region of the spectral peak, large uncertainties result from attempts to calculate these coefficients independently.

Cardioid model fit. We used an approximate but stable method to interpret the 20-MHz data and to check the 13-MHz results. The directional ocean-wave spectrum was represented as the product of the nondirectional spectrum and a cardioid directional factor

$$S(k, \theta) = \frac{g(k)\cos^s[(\theta - \theta_s/2)]}{\mathrm{A(s)}} \tag{28}$$

where $A(s)$ is given in (16). The values of the spreading factor s and mean angle θ_s were set to the average values given by integral inversion ($s = 16$, $\theta_s = 259°$T). Wave numbers were selected to span the spectral peak, and the corresponding Doppler shift $\omega_{m,m'}$ for a given side band was then calculated from the dispersion equation. The ratio $R_{m,m'}$ at this frequency was then obtained by interpolating the experimental values. An estimate of the nondirectional spectrum follows from the equation

$$g_{m,m'}(k) = \frac{R_{m,m'}A(s)}{2\int_{-\pi}^{\pi} |\Gamma_{m,m'}(\theta)|^2 \cos^s[(\theta - \theta_s/2)]d\theta} \tag{29}$$

Estimates from the four side bands should be consistent if the model provides a reasonable fit to the data; Table 10 gives an example for 20 MHz. At the spectral peak and for higher wave numbers, the agreement is within 25%. The four estimates were averaged and were converted to the temporal spectral values plotted in Figure 10. These results confirm those derived by integral inversion.

Comparison with surface data. At the time of the experiment, ocean waves generated by high winds about 1000–1700 km offshore had just arrived at the coast. According to visual observations, waves as high as 20 feet were arriving from slightly south of west.

A pitch-and-roll wave buoy operated by R. Stewart of Scripps Institution of Oceanography was deployed in the third radar range cell. The buoy contains an accelerometer and two inclinometers, producing measurements of orthogonal surface slopes and elevation. The signal-to-noise ratios of the two instruments were approximately 15 and 8 dB, respectively. The buoy provides the first five Fourier coefficients of the ocean-wave spectrum as functions of ocean-wave frequency. The records provided span the period 1200–1444 PST, with a frequency resolution of 3×10^{-4} Hz; each spectral point contains 128 degrees of freedom. Corresponding statistical uncertainties in the Fourier coefficients for the buoy are derived by *Barrick and Lipa* [1979*b*]. In Appendix C we describe how the

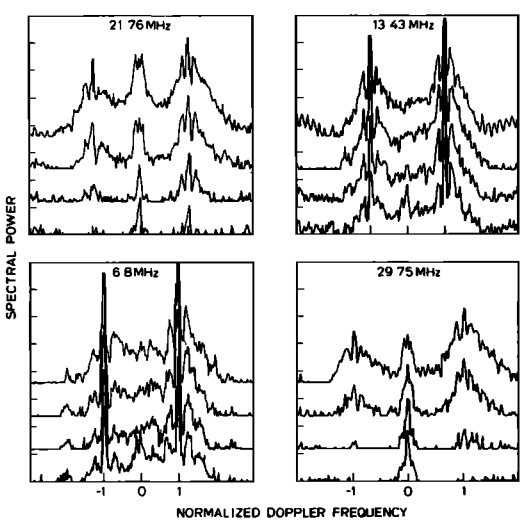

Fig. 8. Spectra measured at Pescadero, January 19, 1978, 1127 PST. Spectra from the different range cells are plotted with the closest range at the top. A 16-point running average has been taken of a 2048-s transform. Vertical tick-marks are separated by 10 dB.

TABLE 9. Results from Peak Frequencies (Pescadero)

Time, PST	Radar Frequency, MHz	Number Averaged	Swell Period, s	Swell Angle, deg T
1130	13.4	160	14.2 ± 0.16	248 ± 4
	21.8	80	13.6 ± 0.24	260 ± 7
	29.8	40	13.4 ± 0.37	250 ± 14
1300	13.4	140	14.4 ± 0.17	264 ± 4
	21.8	90	14.5 ± 0.28	263 ± 8
	29.8	55	14.2 ± 0.41	277 ± 15
1400	13.4	120	14.8 ± 0.18	265 ± 4
	21.8	80	14.2 ± 0.27	263 ± 8
	29.8	55	14.2 ± 0.41	268 ± 14

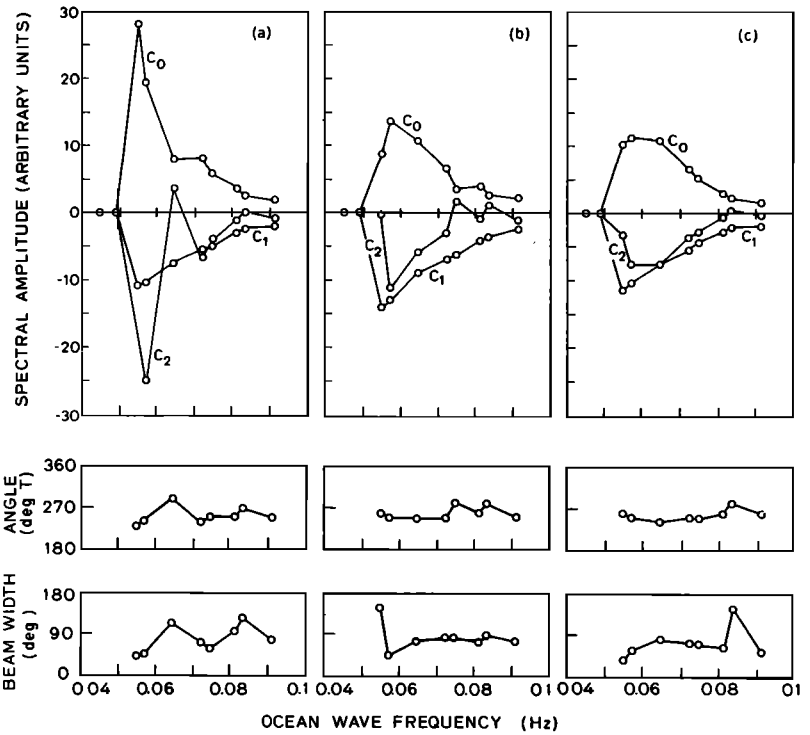

Fig. 9. The first three Fourier coefficients of the ocean wave spectrum determined by integral inversion of radar spectra measured at Pescadero. Direction and beamwidth were obtained by interpretation of these coefficients in terms of a cardioid model; (*a*) 1127–1238 PST, (*b*) 1258–1403 PST, (*c*) 1404–1604 PST.

buoy output was interpreted to give the temporal spectrum in shallow water, mean direction, and the half-power beamwidth of the ocean-wave directional distribution. For purposes of comparison, we averaged the radar results obtained from integral inversion over the time period 1127–1604 PST, and considered radar and buoy parameters for ocean waves with periods greater than 10 s. To obtain an equivalent spectral resolution, both data sets were averaged over frequency bands of width 0.005 Hz. Averaging over bands was necessary for a meaningful comparison, as the frequency resolution of the ocean wave spectrum obtained by inversion was not uniform and differed from that of the buoy measurements. Measured temporal spectra are compared in Figure 12: Spectra measured by the radar and buoy differ slightly in shape, probably owing to smearing of the radar spectrum. The wave heights measured by radar and accelerometer are almost identical. The inclinometer spectrum is consistently greater than the accelerometer spectrum because of the higher noise-power level in the instrument. Results for direction and beamwidth are compared in Figure 13: The wave direction given by the buoy is consistently from further north than that measured by the radar; this may be because the radar and the buoy are producing point and areal measurements, respectively. The beamwidth obtained by the radar is larger than the buoy value, owing to the finite beamwidth of the radar (25° at 13 MHz). We have attempted to derive the true beamwidth of

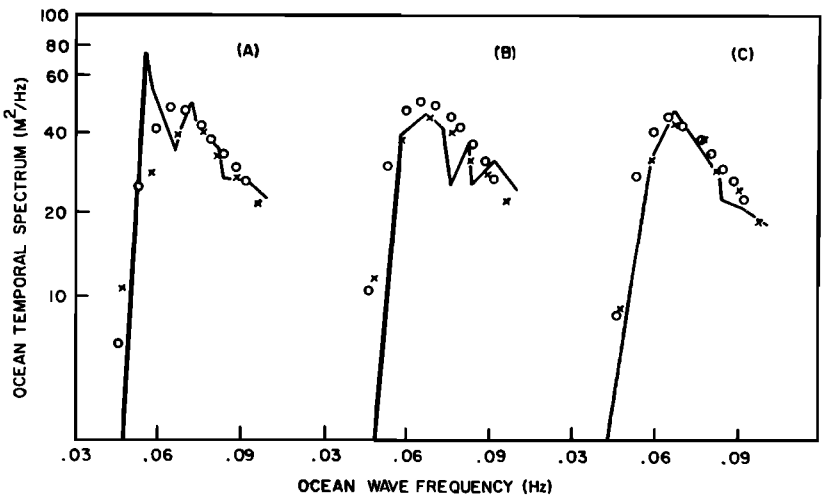

Fig. 10. Ocean temporal spectra derived from the Pescadero data (*a*) 1127–1238 PST, (*b*) 1258–1403 PST, (*c*) 1404–1604 PST. Solid line denotes the integral inversion of 13.4 MHz data; open circle, cardioid model fit to 13.4 MHz data; and crosses, cardioid model fit to 21.8 MHz data.

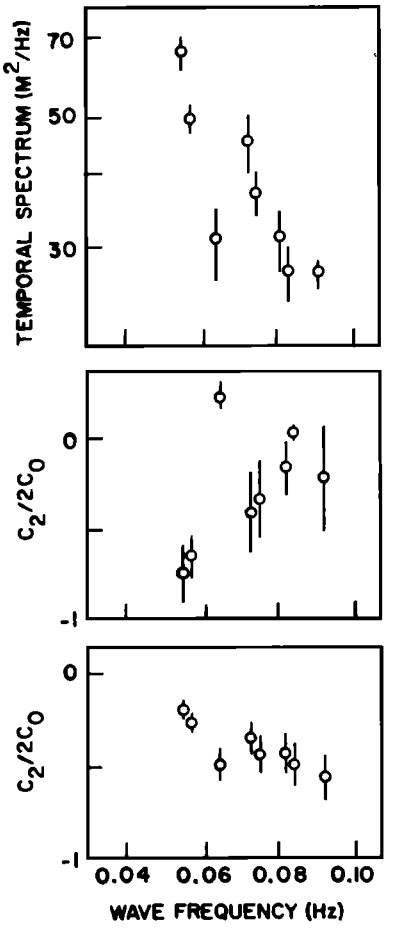

Fig. 11. Statistical uncertainties in ocean parameters derived by integral inversion for the time period 1127–1238 PST. Each error bar represents the standard deviation derived from the random sea-surface height statistics by linear propagation through the inverse transformation.

the ocean-wave directional distribution by using models of the latter; the result however depends on the specific form of the model for the radar-beam pattern. A more exact approach would include the shape of the radar beam in the integral equation before inversion, as was done by *Barrick and Lipa* [1979*b*] for another antenna system.

The temporal spectra were integrated to give the mean-square wave height. Estimates of the centroid frequency and mean direction were obtained by weighting the values at each frequency by the spectral amplitude at that point; the period

TABLE 10. Nondirectional Spectrum from the Four Sidebands (Carbioid Model) 20 MHz, 1130 PST (Pescadero)

Ocean Wave Frequency, Hz	Nondirectional Spectrum, m^{-4}			
	$m = m' = 1$	$m = m' = -1$	$m = -1, m' = 1$	$m = 1, m' = -1$
0.034	2150	0	0	1630
0.047	3960	3390	4010	2460
0.058	8260	7420	9040	5310
0.067	6210	5870	6010	4560
0.075	4100	3490	3150	2800
0.082	2420	2050	1670	1810
0.089	1530	1330	1050	1210
0.095	940	899	698	839
0.101	611	608	526	702
0.106	448	468	442	544

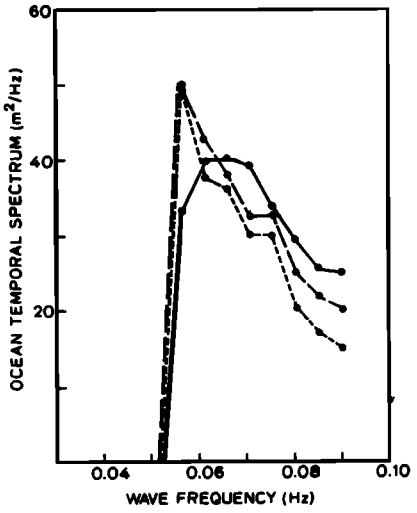

Fig. 12. Comparison of ocean wave temporal spectra measured by radar and buoy at Pescadero. Solid line denotes the integral inversion of 13.4 MHz radar data, 1127–1604 PST, dotted line, accelerometer, 1200–1444 PST; and dashed line, inclinometers, 1200–1444 PST.

was taken as the reciprocal of the centroid frequency. These values are given in Table 11 for the different methods, with statistical uncertainties computed from the χ^2 statistics of the sea-echo spectral power.

Because of initial difficulties in the interpretation of the tilt buoy output, a hindcast of wave conditions was obtained from OSI Inc. Parameters obtained from the several swell components are shown in Table 11. Analogous to the San Clemente experiment, composite values here were formed as follows: The total mean-square wave height was taken as the sum of the individual components, and the direction and frequency were found by weighting the values for each individual component by the mean-square wave height as in (21). The large uncertainties in the hindcast values are derived in Appendix A.

5. CONCLUSIONS

Analysis of experimental HF radar data—based on methods presented in *Lipa and Barrick* [1980]—demonstrates the validity of our theoretical solutions for second-order sea echo and also shows that the important long-wave directional parameters can be extracted to an accuracy exceeding that of the alternate techniques available for comparisons. This paper

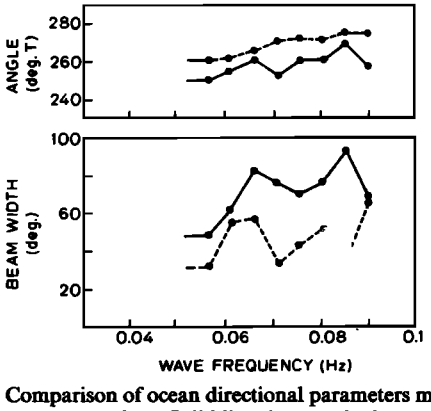

Fig. 13. Comparison of ocean directional parameters measured by radar and buoy at Pescadero. Solid line denotes the integral inversion of 13.4 MHz radar data, 1127–1604 PST; dotted line, pitch and roll wavebuoy, 1200–1444 PST.

TABLE 11. Pescadero Comparisons with Surface Data 1130–1600 PST, January 19, 1974

Source	rms Wave Height, cm	Period, s	Direction, deg T
Radar (inversion of 13 MHz data)	113 ± 4	13.9 ± 0.1	259 ± 1.5
Buoy accelerometer	113 ± 2	13.1 ± 0.1	267 ± 1
Buoy inclinometer	120 ± 2	14.2 ± 0.1	267 ± 1
Hindcast	117 ± 56	14.0 ± 2	275 ± 24

has concentrated on data sets originating from narrow-beam radars, since the mathematical techniques for that case lead to the most straightforward demonstration of these claims. The features of the present analysis that strengthen these conclusions are the following:

1. Three separate experiments were analyzed; one from a skywave system and two from different surface-wave radars.
2. In all cases, simultaneous radar operation on multiple frequencies and separate analyses of the data obtained yielded consistent long-wave parameters. In two cases, the frequency region of operation spanned nearly three octaves; this demonstrates that successful utilization of the techniques does not depend on judicious selection of the operating frequency.
3. In the case of the NOAA San Clemente Island experiment, data from two simultaneous narrow beams were successfully analyzed.
4. Long-period wave information has been extracted both when the shorter-period wind waves predominated (i.e., the NOAA experiment) and when the long waves predominated (i.e., the other two experiments).
5. Significant wave heights of the long waves varied considerably among the three experiments, from 0.75 to 4.57 m.
6. Two swell components from different directions but lying within the same resolvable frequency band were detected and verified, in the case of the NOAA experiment.
7. All radar-deduced wave-parameter accuracy claims have been supported by independent surface observations: the NOAA EB-20 data buoy in the case of the SRI WARF experiment, a Datawell Waverider buoy for the NOAA San Clemente Island experiment, and the Scripps tilt buoy for the Stanford Pescadero experiment. As supplementary information, at least one wave hindcast was done by an independent company for each experiment and used in the comparisons. (Two separate hindcasts were used for the SRI Warf experiment.) Although uncertainties in the hindcast values are large, they are useful for the following reasons: In the case of the SRI Warf and NOAA San Clemente experiments, hindcasts provided the only directional surface information for comparison with the radar results; for the Stanford Pescadero experiment, a hindcast was obtained because the radar results indicated errors in the tilt buoy calibration which was subsequently corrected. As a general conclusion, the discrepancies between the different observations are explained by the uncertainties.
8. At least three mathematical techniques were used for extracting long-wave parameters from the second-order result for sea scatter; at least two were applied simultaneously to the same data sets, producing consistent results.
9. The dominant ocean wave-to-radar look direction varied widely among the experiments: from 0° to 52°. Thus good agreement is not a fortuitous result of looking in the right direction.
10. The radar methods have been demonstrated for long waves observed in shallow water, as well as in deep water. In the Stanford Pescadero experiment, application of the proper depth correction factor of ~1.7 to the deep-water dispersion equation for both radar and buoy data at the spectral peak produced remarkable agreement.
11. In all, over 5000 independent radar data samples have been employed in the above analyses. These were used to estimate errors in the wave parameters. Hence, success is not being claimed based on fortunate agreement of a handful of points.
12. The theoretical solution for second-order scatter—used as the basis for the analyses here—contains no unknown parameters. Hence there is no arbitrary sliding of curves to obtain a 'best fit.' Even unknown path losses and system gains are removed by an exact process of dividing the second-order echo by the first-order echo energy.

Two other theoretical models for higher-order sea-echo Doppler spectra have been suggested. In one, *Ward* [1969] proposes that this higher-order echo is produced by spatial harmonics attached to some dominant fundamental wave; the Doppler spectra would thus consist of peaks at $\sqrt{n}$ times the Bragg peak frequency, where n is the spatial harmonic. In another model, *Trizna et al.* [1977] suggest that a simple electromagnetic 'corner-reflector' effect accounts for the entire second-order echo, and they recommend that an experiment be done to verify this proposed theory. The three experiments analyzed herein conclusively prove that those two suggested theories cannot adequately explain second-order scatter and hence cannot be employed to extract usefully sea-state information. In the first place, those models do not agree with our second-order scatter solution that has been derived from the governing physical equations describing the surface processes. Second, since our theory produces close agreement with surface observations under such a wide variety of experimental conditions, it alone can be considered to have been validated in any manner.

One question remains inadequately answered. This is the effect of third-order contributions to the Doppler spectrum at considerably higher radar frequencies (VHF) and/or sea states. For the reasonably high sea states and for the upper HF region employed here, we found no evidence of contamination by third-order processes. Preliminary analyses indicate that third-order effects should not have been seen for the situations we encountered here. However, how much higher the frequency and sea state can be before such contamination occurs is still an open question.

It was mentioned that there is some problem in accurately separating the directional Fourier angular coefficients c_0 and c_2 for higher radar frequencies and for longer waves. Although this problem is alleviated for the shorter waves, other computational problems will be encountered at upper HF for waves with periods less than ~8 s. The linearization approximation that works so well for the integral equation here becomes less valid for these shorter waves. Therefore, we are developing and testing techniques for inverting the integral equation in the short-wave region that do not employ this approximation.

Finally, we note that the narrow-beam HF antenna systems considered here are generally very large and expensive structures, requiring a considerable area of land for their deployment. Also, a single narrow-beam radar cannot measure the odd Fourier coefficients of the ocean-wave spectrum. We are now testing a compact HF loop-antenna arrangement that

forms a broad beam which is scanned electronically in the received-signal processing [*Barrick and Lipa,* 1979*b*]. In addition to being inexpensive and transportable, this radar is expected to provide the first five Fourier coefficients as a function of ocean-wave frequency to give information equivalent to a pitch-and-roll wave buoy.

APPENDIX A: WAVE HINDCAST ACCURACY ASSESSMENT

In this appendix we show how to estimate errors in hindcasts based on the methods of *Pierson et al.* [1953] as used by OSI, Inc., in obtaining the hindcast results quoted in the text. This is required to permit meaningful comparisons with radar observations.

The primary errors in wind-wave hindcasts result from uncertainties in the wind-field itself, and these are considerable. Since there were insufficient wind observations over the oceans to construct a high-quality field of streamlines, pressure charts showing isobaric contours were employed to give the geostrophic wind speed and direction. The largest possible rectangle was then located over a nearly parallel section of closely spaced isobars, such that wind speed and direction varied by no more than 10% and 15° within the box. The duration of the wind and its speed are then used to calculate wave height and period within the box from empirically determined charts. Simple wave-energy propagation considerations then allow waves generated within this box to be propagated to other desired areas.

Errors occur owing to uncertainty in the centers of the pressure field itself (e.g., the lows or storm centers, and highs, around which isobars are contoured). *Parsons* [1979] studied these locational errors over the ocean. His studies imply that the boxes used to generate hindcasts can be mispositioned by as much as 500 km. This uncertainty translates into errors in (1) mean-wave direction, (2) arrival time of the waves, and hence (3) the mean-wave period at a given location. We have employed this 500-km positional uncertainty to estimate errors in wave period and direction.

Marine experiments [*Petterssen,* 1956] show that wind speed does not follow the simple geostrophic balance, but is typically only 2/3 of that value (owing to frictional effects near the surface). More important, however, is the fact that the wind speed standard deviation is ~24% of the mean value. This uncertainty in wind speed translates into wave height errors, particularly for the longest-period waves generated within the box.

We trace through an example of estimating wave hindcast errors for the Stanford Pescadero experiment. A hindcast procured from OSI, Inc., (located in Santa Barbara, California) showed that the dominant waves at Pescadero on January 19, 1978, of period greater than 10 s came from a prior offshore storm. The generating 'box' for these waves was 650 km wide by 740 km long, centered 1250 km from the radar site. Although the storm had dissipated at the time of the radar observations, the generating area was so close that the swell was spread considerably in angle and period (e.g., over a 40° angular beamwidth). Assuming that the lateral positional error of the box at 1250 km could have been ±500 km, one obtains a mean wave directional error of ±25°. A distance error in position of ±500 km means that 14-s waves could have arrived ±12 hours from the predicted time. From the hindcasted table of arrival times for different frequency components of the wave spectrum, this gives a period error of ±2 s. Wave height error is less straightforward because factors such as fetch and duration influence wave height as well as wind speed. However, by using the relationship that relates wave height to wind speed squared for infinite fetch and fully developed seas means that a ±24% error in wind speed translates to a ±48% error in wave height; since hindcast rms wave height was 117 cm, we thus obtain an error estimate of ±56 cm. In addition, a 24% error in wind speed means that spectral components with periods as long at 17 s could have been generated (the hindcast showed no wave energy beyond 14 s). Both the radar and the buoy observed appreciable wave energy out as far as 16.5 s, consistent with the magnitude of hindcast errors.

Because of many other oversimplifications employed in the overall hindcasting process, it is probably not meaningful to attempt to estimate these errors more accurately.

APPENDIX B: LOGARITHMIC NORMALIZATION OF HF DOPPLER SPECTRA

In this appendix we briefly describe a method of combining or of averaging independent Doppler spectra (to maximize the number of degrees of freedom in the composite spectrum) that permits removal of unknown multiplicative path-loss or system gain factors from each spectrum. A detailed derivation is given by *Barrick* [1980]. For each individual spectrum a frequency window is defined to include the region which has an adequate signal-to-noise ratio. The lth spectrum is then normalized by the factor

$$C_l = \exp\left\{\frac{1}{N}\sum_{n=1}^{N} \ln P_n^l\right\} \tag{B1}$$

where N is the number of spectral points included in the window and P_n^l is the power of the nth spectral point. The composite result is obtained by summing the normalized spectra

$$P_n = \sum_{l=1}^{L} P_n^l / C_l \tag{B2}$$

Assuming P_n^l to obey χ^2 statistics with $2K$ degrees of freedom (i.e., the number of independent power spectral samples averaged is K), the standard deviations in P_n are given by

$$Sd(P_n) = 1/\sqrt{LK_e} \tag{B3}$$

where $2K_e$ defines the number of degrees of freedom; this has the following approximate form for values of K greater than 10, which applies to the cases treated in this paper,

$$K_e \approx \frac{K-1}{1+(1+2.5/K)/J}. \tag{B4}$$

APPENDIX C: INTERPRETATION OF PITCH-AND-ROLL WAVEBUOY OUTPUT IN SHALLOW WATER

The buoy contains and accelerometer for the measurement of surface elevation ζ_1 and two inclinometers for the two components of surface slope ζ_2 and ζ_3. Results provided consist of the cospectra (C_{ij}) and quad-spectra (Q_{ij}) between ζ_1, ζ_2, and ζ_3, given as a function of angular frequency ω. *Tyler et al.* [1974] give the relationships between these spectra and the directional ocean-wave spectrum $S(k, \theta)$ at wave number k and angle θ:

$$C_{11}(\omega) = \int_{-\pi}^{\pi} S(k, \theta)\, d\theta \qquad Q_{12} = k \int_{-\pi}^{\pi} \cos\theta\, S(k, \theta)\, d\theta$$

$$C_{22}(\omega) = k^2 \int_{-\pi}^{\pi} \cos^2\theta\, S(k, \theta)\, d\theta$$

$$Q_{13} = k \int_{-\pi}^{\pi} \sin\theta\, S(k, \theta)\, d\theta$$

$$C_{33}(\omega) = k^2 \int_{-\pi}^{\pi} \sin^2\theta\, S(k,\theta)\, d\theta \tag{C1}$$

The wave number k corresponding to a given frequency follows from numerical solution of the shallow-water dispersion equation

$$\omega^2 = gk \tanh(kd) \tag{C2}$$

Two estimates of the temporal spectrum at frequency f (equal to $\omega/2\pi$) follow from (C1); from the accelerometer

$$F(f) = C_{11}(\omega)/2\pi \tag{C3}$$

and from the inclinometers

$$F(f) = \frac{C_{22}(\omega) + C_{33}(\omega)}{2\pi k^2(\omega)} \tag{C4}$$

where $k(\omega)$ is obtained from solving (C2). An estimate of the mean angle was obtained from the relation

$$\theta(\omega) = \tan^{-1}[Q_{12}(\omega)/Q_{13}(\omega)] \tag{C5}$$

and the half-power beamwidth obtained by fitting a cardioid model as described by *Barrick and Lipa* [1979*b*]

$$\Delta\theta(\omega) = 4\cos^{-1}\left[\left(\frac{1}{2}\right)^{2-\mu_1/2\mu_1}\right] \tag{C6}$$

where

$$\mu_1 = \left[\frac{Q_{12}(\omega) + Q_{13}(\omega)}{C_{11}(\omega)}\right]^{1/2} \tag{C7}$$

Acknowledgments. This work was supported by NOAA under contracts 03-78-B01-119 and 03-7-022-35111 and ONR under contract N00014-75-C-0356. We are grateful to C. C. Teague and E. C. Ha who provided the radar spectra from the Pescadero experiment, to R. H. Stewart for providing the tilt buoy data, and to H. T. Howard for coordinating the Stanford experiment.

REFERENCES

Barrick, D. E., Dependence of second-order sidebands in HF sea echo upon sea state, *IEEE G-AP Int. Symp. Digest*, 194–197, 1971.

Barrick, D. E., Remote sensing of sea state by radar, in *Remote Sensing of the Troposphere*, edited by V. E. Derr, U.S. Government Printing Office, Washington, D. C., 1972.

Barrick, D. E., Extraction of wave parameters from measured HF sea-echo Doppler spectra, *Radio Sci., 12*, 415–424, 1977.

Barrick, D. E., Logarithmic normalization of sea-echo spectra, *Tech. Memo. ERL WPL-56*, Nat. Oceanic Atmos. Admin., Boulder, Colo., 1980.

Barrick, D. E., and B. J. Lipa, Ocean surface features observed by HF coastal ground-wave radars: A progress review, in *Ocean Wave Climate*, Plenum, New York, 1979*a*.

Barrick, D. E., and B. J. Lipa, A compact transportable HF radar system for directional coastal wave-field measurements, in *Ocean Wave Climate*, Plenum, New York, 1979*b*.

Barrick, D. E., J. M. Headrick, R. W. Bogle, and D. D. Crombie, Sea backscatter at HF: Interpretation and utilization of the echo, *Proc. IEEE, 63*, 673–680, 1974.

Hasselmann, K., Determination of ocean wave spectra from Doppler radar return from the sea surface, *Nature Phys. Sci., 229*, 16–17, 1971.

Lipa, B. J., Inversion of second-order radar echoes from the sea, *J. Geophys. Res., 83*, 959–962, 1978.

Lipa, B. J., and D. E. Barrick, Methods for the extraction of long ocean wave parameters from narrow-beam HF radar sea echo, *Radio Sci., 15*, 843–853, 1980.

Maresca, J. W., Jr., and T. M. Georges, Measuring rms waveheight and the scalar ocean wave spectrum with HF skywave radar, *J. Geophys. Res., 85*, 2759–2771, 1980.

Parsons, C. L., Geos 3 waveheight measurements: An assessment during high sea state conditions in the North Atlantic, *J. Geophys. Res., 84*, 4011–4020, 1979.

Petterssen, S., *Weather Analysis and Forecasting, vol. 1*, McGraw-Hill, New York, 1956.

Pierson, W. J., A. Neumann, and R. W. James, Practical methods for observing and forecasting ocean waves by means of wave spectra and statistics, *HO Pub 603*, U.S. Navy, Washington, D. C., 1953.

Trizna, D. B., J. C. Moore, J. M. Headrick, and R. W. Bogle, Directional sea spectrum determination using HF Doppler radar techniques, *IEEE J. Oceanic Eng., 2*, 4–11, 1977.

Tyler, G. L., C. C. Teague, R. H. Stewart, A. M. Peterson, W. H. Munk, and J. W. Joy, Wave directional spectra from synthetic aperture observations of radio scatter, *Deep Sea Res., 21*, 989–1016, 1974.

Ward, J. F., Power spectra from ocean movements measured remotely by ionospheric radio backscatter, *Nature, 223*, 1325–1330, 1969.

Withee, G. W., and W. C. Blasingame, Environmental data quality estimates for ocean data buoys, *IEEE Oceans '76*, 1976.

(Received April 2, 1980;
revised September 8, 1980;
accepted September 17, 1980.)